GA–A28180

ROTATIONAL SHEAR EFFECTS ON EDGE HARMONIC OSCILLATIONS IN DIII-D QUIESCENT H-MODE DISCHARGES

By

X. Chen[1], K.H. Burrell[1], N.M. Ferraro[1], T.H. Osborne[1], M.E. Austin[2], A.M. Garofalo[1], R.J. Groebner[1], G.J. Kramer[3], N.C. Luhmann, Jr.[4], G.R. Mckee[5], C.M. Muscatello[1], R. Nazikian[3], X. Ren[4], P.B. Snyder[1], W.M. Solomon[3], B.J. Tobias[3], And Z. Yan[5]

This is a preprint of a paper to be submitted for publication in Nuclear Fusion.

[1]General Atomics
[2]University of Texas
[3]Princeton Plasma Physics Laboratory
[4]University of California
[5]University of Wisconsin

This work was supported in part under the auspices of the U.S. Department of Energy (USDOE) under DE-FC02-04ER54698[1], DE-FG03-97ER54415[2],DE-AC02-09CH11466[3], DE-FG02-99ER54531[4], and DE-FG02-08ER54999[5]. DIII-D data shown in this paper can be obtained in digital format by following the links at https://fusion.gat.com/global/D3D_DMP.

GENERAL ATOMICS PROJECT 30200

SEPTEMBER 2015

GENERAL ATOMICS

Rotational Shear Effects on Edge Harmonic Oscillations in DIII-D Quiescent H-mode Discharges

Xi Chen,[1] K.H. Burrell,[1] N.M. Ferraro,[1] T.H. Osborne,[1] M.E. Austin,[2] A.M. Garofalo,[1] R.J. Groebner, [1] G.J. Kramer, [3] N.C. Luhmann, Jr.,[4] G.R. McKee,[5] C.M. Muscatello,[1] R. Nazikian, [3] X. Ren, [4] P.B. Snyder,[1] W.M. Solomon,[3] B.J. Tobias, [3] Z. Yan[5]

[1]*General Atomics, PO Box 85608, San Diego, CA 92186-5608, USA*

[2]*Institute for Fusion Studies, University of Texas-Austin, Austin, TX 78712, USA*

[3]*Princeton Plasma Physics Laboratory, PO Box 451, Princeton, NJ 08543, USA*

[4]*Department of Applied Science and Department of Electrical and Computer Engineering, University of California-Davis, Davis, CA 95616, USA*

[5]*Department of Engineering, University of Wisconsin-Madison, Madison, WI 58705, USA*

In the quiescent H-mode (QH-mode) regime, edge harmonic oscillations (EHO) play an important role in avoiding transient edge localized mode (ELM) power fluxes by providing benign and continuous edge particle transport. A detailed theoretical, experimental and modeling comparison has been made of low-n ($n \leq 5$) EHO in DIII-D QH-mode plasmas. The calculated linear eigenmode structure from the extended MHD code M3D-C1 matches closely the coherent EHO properties from external magnetics data and internal measurements using the ECE, BES, ECE-Imaging and microwave imaging reflectometer (MIR) diagnostics, as well as the kink/peeling mode properties found by the ideal MHD code ELITE. Numerical investigations indicate that the low-n EHO-like solutions from M3D-C1 are destabilized by the rotation and/or rotational shear while high-n modes are stabilized. This effect is independent of the rotation direction, suggesting that EHO can be destabilized in principle with rotation in either direction. The modeling results are consistent with observations of the EHO, support the proposed theory of the EHO as a low-n kink/peeling mode destabilized by edge ExB rotational shear, and improve our understanding and confidence in creating and sustaining QH-mode in present and future devices.

I. Introduction

In toroidal plasma devices, a high confinement mode of plasma operation (H-mode) is often accompanied by edge-localized modes (ELMs) driven by the high pressure gradient of the H-mode pedestal [1]. ELMs induce periodic and impulsive particle transport, which can help prevent impurity accumulation and sustain plasma performance. However, the intensive heat pulses arising from large ELMs will be detrimental to the vacuum vessel, divertor and plasma facing components in future devices [2]. Consequently, elimination or mitigation of these large ELMs while retaining good thermal confinement and sufficient edge particle transport for impurity control is necessary for next step devices such as ITER [3]. One potential solution is quiescent H-mode (QH-mode) [4,5], which exhibits stationary operation with an H-mode edge pedestal, good thermal confinement and particle transport for impurity removal [6], but without detrimental ELMs.

QH-mode operation is generally accompanied by a coherent edge-localized low-toroidal (n) mode number MHD oscillation, which has multiple harmonics and is known as the edge harmonic oscillation (EHO). Previous studies have demonstrated that the EHO produces electron, main ion, and impurity particle transport at the plasma edge stronger than the ELMs under similar conditions [6,7], as well as energy and momentum transport; however, the H-mode pedestal pressure and core thermal confinement in QH-mode is comparable to ELMing H-mode. It has been found experimentally that the EHO provides a continuous transport channel that maintains the plasma profiles at conditions just below the ELM stability boundary [9,10]. Consequently, understanding the physics of the EHO is important for expanding the QH-mode operation regime and further improving the confinement performance.

The EHO is thought to be a kink/peeling mode partially driven by rotational shear, the associated self-transport of momentum or damping of rotation leading to a saturation rather than explosive process [8, 11]. QH-mode is usually obtained under conditions of low H-mode pedestal collisionality (ν_{*e}<0.3) with strong plasma shaping and higher edge safety factor (q_{95}>5). Under these conditions, the pedestal approaches the low-n current density driven kink/peeling branch of the peeling-ballooning mode, which would

normally trigger an ELM. Previous experiments have shown that ramping down the plasma current can turn off the EHO while ramping up the plasma current can trigger ELMs in QH-mode discharges [7, 12]. Stability analysis also shows that the QH-mode pedestal lies near to, but somewhat below, the low-n kink/peeling stability boundary when rotation effects are excluded [10, 12]. These indicate that the EHO is partially a current density driven instability but has a threshold lower than that of a purely current density driven peeling mode (i.e., low-n current density driven ELM), suggesting the possibility of an additional drive mechanism.

Theory and experiments suggest that large edge ExB rotational shear is this additional drive mechanism of the EHO. Single fluid ideal MHD peeling-ballooning mode calculations have shown that the toroidal rotational shear is stabilizing for high-n modes and destabilizing for low-n modes [8]. Experimentally, strong neutral beam injection (NBI) has long been required to generate the strong toroidal rotation, thus strong rotational shear, in order to excite the EHO. At too low rotational shear, EHOs disappear and ELMs appear [13]. QH-mode favors neutral beam injection in the direction counter to the plasma current. The toroidal rotation produced by this NBI direction reinforces the diamagnetic rotation in determining the radial electric field from radial force balance. Indeed, QH plasma is found to have a significantly deeper well in the edge radial electric field (E_r) than in the ELMy H-mode [4,9,12,14]. A detailed analysis of the E_r profile in QH-mode and H-mode plasmas suggests that the shear in the toroidal rotation associated with ExB drift (ω_E) is more important for entering the QH-mode than the carbon toroidal rotation (a proxy for the toroidal flow used in the single fluid ideal MHD theory of EHO) [15]. QH-mode indeed has been sustained with both NBI torque and toroidal rotation near zero on DIII-D where the strong edge ω_E shear is conserved with the torque from applied non-axisymmetric non-resonant magnetic fields [13, 15]. Based on the experimental observations, a model has been proposed for QH-mode in which an ω_E driven low-n kink/peeling mode reaches saturation through relaxation of the ω_E shear rather than growing explosively like an ELM.

In previous studies, the ELITE code [16,17] has been used to compute peeling-ballooning stability in QH-mode discharges. However, because the ELITE code uses a large n expansion, it is not accurate at very low n (i.e. 1–3), while the dominant toroidal

mode number is typically $n \leq 3$ for the EHO. Although the rotational shear can be included in ELITE, the effect of rotation, for example in terms of interaction with the conducting boundary, is not included, which can impact the low-n stability. QH-mode experimentally favors a small gap between the plasma and the vacuum vessel on the low field side, which may enhance the rotational shear through the resistive wall dragging on the low-n EHO. As a result of these limitations, a comparison of the measured EHO structure with the prediction has not previously been carried out.

In the present paper, we apply the M3D-C1 [18] code, which solves the resistive MHD equations in fully 3D toroidal geometry, and includes the effect of the conducting wall, the SOL plasma, and rotational effects on the mode stability. For this study, M3D-C1 was run in linear, single-fluid mode as an initial value computation including toroidal mode numbers down to n=1. In the numerical investigation of the rotational shear effects, experimental ExB rotation profiles are used in the modeling instead of toroidal plasma rotation profiles that were used in previous studies [8, 19]. As discussed in the following sections, we find good agreement between the characteristics of the EHO as measured on a number of diagnostics with the low-n M3D-C1 solutions obtained using the experimental profiles and the kinetic equilibrium as inputs. This result further supports the idea of the EHO as a saturated edge kink/peeling mode with the ExB rotational shear as an additional drive mechanism down to n=1.

The paper is organized as follows: Section II presents the details of the equilibrium profiles and typical properties of QH-mode discharges with a strong coherent EHO. Section II presents the modeling of low-n (<5) kink/peeling modes with M3D-C1 and compares the results with the ELITE predictions. Comparison with experimental profiles of fluctuations in magnetic field, density, and temperature measured by various diagnostics are also shown in section II. Section III examines the effects of the rotation profile on the M3D-C1 modeling and results are compared with experimental quantities. Section IV summarizes and discusses the results.

II. Mode Structure Modeling and Comparison with Experiments

1. Experimental setup and key diagnostics

Time traces for a typical DIII-D QH-mode discharge #157102 are shown in figure 1. This discharge is used for comparison with modeling results in much of the discussion that follows. It is a neutral beam heated deuterium plasma with the toroidal magnetic field (B_T ~ 2.06 T) and the plasma current (Ip ~ 1.1 MA) in the B_T direction and a safety factor of q_{95} ~ 5.4. On DIII-D, the QH-mode has been seen with injected power from 3 MW up to 15 MW (the maximum power is set by the core beta limit). In discharge 157102, at t ~ 1040 ms shortly after the L-H transition, the QH-mode is entered with 6.2 MW neutral beam injection (NBI) [figure 1(a)]. The NBI direction is opposite to the plasma current direction (counter-injection) producing the strongest edge rotation and rotational shear; the modulation in NBI is used for diagnostic purpose. The total radiated power [figure 1(a)], line-integrated density [figure 1(b)], pedestal density [figure 1(c)], core and edge temperature remain nearly stationary. The coherent EHO starts at t ~ 1040 ms and is clearly visible on the edge magnetic sensors [figure 1(d)] and on several other diagnostics. Between 1540 and 1580 ms following an ELM indicated by the large spike in the D-alpha signal [figure 1(e)], the EHO disappears and the discharge briefly drops out of QH-mode. The impact of the EHO on particle transport is indicated by the rise in pedestal density [figure 1(c)] during this period when the EHO is off. This brief return to standard H-mode occurs as the plasma is shifted from upper single null (USN) to double null (DN) divertor configuration between 1500 and 1600 ms, which also accounts for the rise in the D-alpha baseline at this time [figure 1(e)], as the D-alpha signal is taken from the lower divertor view.

QH-mode on DIII-D can be robustly obtained with good divertor cryopumping to produce low pedestal density and electron collisionality. The collisionality is proportional to the cube of the density at fixed pressure. The electron collisionality ν_{*e} is about 0.2 during the QH-mode phase of the discharge shown in figure 1. Low collisionality is favorable for QH-mode as this maximizes the pedestal bootstrap current for a given pressure gradient to access the low-n kink/peeling branch of the peeling-ballooning mode where rotation is destabilizing, rather than to the higher-n ballooning mode branch. (It should be noted that QH-mode can be obtained with pedestal densities as high as n_{e_ped} = 6.5 x10^{13} cm^{-3} [20] but not as robustly.) As usual for QH-mode on DIII-D, the deuterium gas filling for the discharge in figure 1 is reduced to the minimum possible while

avoiding runway electrons and is turned off completely after the L-H transition. Low pedestal density is maintained, i.e. $n_{e\_ped} \sim 1.1 \times 10^{13}$ cm^{-3} for the QH phase shown in figure 1(c).

Strong plasma shaping is another requirement for QH-mode operation. Both the maximum density at which the pedestal is limited by low-n kink/peeling mode and the pedestal pressure at the stability limit increase with increased triangularity and elongation. The discharge shown in figure 1 is a highly shaped, near balanced double-null (figure 2), with elongation $\kappa \sim 1.9$, and average triangularity $\delta \sim 0.58$. The magnetic axis is at R ~ 177 cm, while the last closed flux surface (LCFS) is at R ~ 227 cm on the low field side midplane, giving a spacing between the plasma and the conducting wall on the low field side midplane (gapout) ~ 9.5 cm, and on the high field side midplane (gapin) ~ 8.2 cm. Also the radial separation on the outer midplane between the flux surfaces connected to the upper and lower divertor X-points (dRsep) is -0.6 cm. The outer strike point is kept at R ~ 136 cm for the best divertor pumping, where the entry to the pump duct is located at R ~ 137.2 cm. Starting from t=1500 ms, the gapout is scanned by ±2 cm at 5 Hz [figure 1(f)], while other plasma parameters are kept constant, to improve spatial resolution of the edge diagnostics as the detection points for many of them, such as the charge exchange recombination system, are spatially fixed. The 5 Hz oscillations associated with the gapout scan are seen in some of the plasma parameters shown in figure 1.

The detailed measurements by a suite of equilibrium and fluctuation diagnostics [figure 2] provide critical information for numerical analysis and modeling of discharge 157102. The high-resolution edge channels of the newly upgraded Thomson scattering (TS) system [21] measure the pedestal electron temperature and density at 500 Hz with spatial resolution of ~0.3 cm in the pedestal region compared to typical pedestal width of 2-3 cm. The charge exchange recombination (CER) spectroscopy system [22, 23] tuned to the dominant carbon impurity wavelength provides ion temperature, plasma rotation speed, and carbon density measurements at 200 Hz with radial resolution of ~0.6 cm in the pedestal compared to typical pedestal width of 1-2 cm in the measurement region. The spatial resolution of TS and CER data are further improved with the edge sweeping technique described above. The DIII-D forty-channel ECE radiometer [24] (not shown in

figure 2) provides full radial profile of electron temperature with a resolution of <2 cm and at up to 500 kHz. Toroidal and poloidal arrays of magnetic sensors [25] (not shown in figure 2) on the inner surface of the vacuum vessel wall measure the local toroidal and poloidal magnetic fields. The magnetic data provide the primary measurement for determination of the mode number of the EHO, especially the toroidal mode number as illustrated later in the paper. At the standard sampling rate, the maximum frequency that can be measured by the magnetic sensors is 100 kHz, which is adequate for resolving the coherent EHO (fundamental frequency and harmonics).

In addition to edge magnetic coils, multiple pedestal fluctuation diagnostics (figure 2) provide internal structures and wavenumber information on the EHO. An ECE-Imaging (ECE-I) [26] system provides time-resolved 2D measurements of electron temperature fluctuations on a finely spaced grid covering up to 55 cm vertically at 8 radial locations. A 64-channel beam emission spectrometer (BES) [27] system measures local density fluctuations using the Doppler shifted collisionally induced D_alpha emission from deuterium atoms of the heating neutral beam. BES measures 1D and/or 2D density fluctuations up to 500 kHz for wavenumbers $k_{perp} < 1.5$ cm^{-1}, corresponding to $k_{perp}*\rho_s < 0.5$ in the pedestal. In discharge 157102, an 8x7 2D array of BES channels is deployed across the pedestal region covering an area of 8 cm (poloidally) by 8 cm (radially) with an additional 8 channel linear array from R = 214 to 222 cm [figure 2]. The poloidal wavenumbers are extracted by correlating poloidally-separated channels. A turbulence decorrelation time is also derived from poloidal correlation functions. A newly installed microwave imaging reflectometer (MIR) [28] also provides time-resolved information about electron density fluctuations in two-dimensions. The DIII-D MIR system is a quasi-optically imaged X-mode microwave reflectometer with twelve vertical sightlines at four density-dependent cutoff surfaces (corresponding to four radial locations). In discharge 157102, the twelve vertically separated sightlines covered from z = -11 cm to +8 cm in the edge with a poloidal resolution of ~3 cm and two out of the four MIR probing frequencies were able to be tuned to measure a ~5 mm wide region in the low field side (LFS) pedestal with a resolution of 2-3 mm.

2. Profile and equilibrium inputs for M3D-C1 and stability analysis

Profiles with high resolution and accuracy in the pedestal region are important for pedestal stability analysis and modeling of edge modes with very fine structure such as the EHO. The analysis and modeling focus on the strong coherent EHO that appears after t=1600 ms in discharge 157102 [Fig 1(d)]. The radial kinetic profiles are obtained using a Python based profile-fitting program [29]. The data points shown in figure 3 and figure 4 are averaged over a 25 ms time window centered at t = 2420 ms. Fits to the data from a 200 ms window are quite similar, owing to the stationary nature of the QH-mode pedestal. At each measurement time point, radial profiles are mapped from physical to poloidal magnetic flux coordinates, using reconstructed EFIT [30] equilibria derived from magnetics data at the measurement time. All individually mapped data within the overall averaging time window are collected and fit as one profile. Modified tanh (mtanh) functions [31] for the pedestal coupled to a spline model for the core are used to fit the electron and ion radial profiles, while the rotation profiles are fit with a spline model from core to pedestal. The electron (ion) pressure is taken to be the product of the electron (ion) density and temperature. The averaged electron profiles and ion/rotation profiles are radially adjusted to satisfy the following two criteria respectively: the electron profiles are shifted so that the electron temperature at the separatrix matches the value determined from a 'two-point' divertor heat flux model [32], for this case, T_{e_sep} = 100 eV; while the ion and rotation profiles are shifted so that, at the separatrix, the radial electric field $E_r = 0$ (or $\omega_E = 0$). The uncertainties of these measurements are also illustrated in figure 4. The error bar of the amplitude of electron properties includes the uncertainty from the photon statistics in the measurements plus a statistical estimate, which is based on the quality of fit to the assumed pedestal profile shape to account for the variability of the measurements and the equilibrium reconstructions among the time points collected to produce the average profiles. The positional (horizontal) error is associated with inaccuracy in the mapping equilibrium at each time point. The error bar in ion properties represents a fixed 10% error due to the larger uncertainty in the measurements and there is no horizontal error bar since the variability in the equilibrium reconstruction generally has little impact on the ion profile fits.

A kinetic EFIT equilibrium is generated by setting the pressure to the experimental total pressure, which is the sum of the measured electron and ion pressures and the fast

ion pressure calculated using the Monte Carlo NUBEAM [33, 34] module in the ONETWO [35] transport code. The flux surface averaged toroidal current density in the core plasma is determined from motional Stark effect (MSE) [36] measurements, while in the pedestal region where the large static radial electric field makes MSE measurement difficult, it is taken to be the sum of the bootstrap current (J_{BS}) computed using the Sauter model [37,38], the neutral beam driven current (J_{NBI}) derived using NUBEAM, and the Ohmic current (J_{OH}) [figure 4(h)]. J_{OH} is determined from the loop voltage and the neoclassical plasma resistance assuming full relaxation, with the loop voltage tuned to give net plasma current same as the measured total plasma current. Generally, the resultant loop voltage agrees with the measured value including the case shown in figure 4(h). Iterations are taken in the fitting process wherein the pressure profile in poloidal flux coordinates is adjusted to account for changes in the mapping between physical and poloidal flux coordinates in order to maintain the gradient of the total pressure in physical space at the experimental value.

The peeling-ballooning mode stability analysis has been performed for this discharge at t = 2420 ms using the ideal MHD ELITE code [16, 17] (figure 5). ELITE is a 2D ideal linear eigenvalue code based on the coupled peeling-ballooning theory. Amongst other things, ELITE returns the growth rate (γ) and 2D eigenmode structure of finite-n ideal MHD modes. The ELITE calculations are carried out in the experimental kinetic equilibrium and in a set of model equilibria with the edge current and the edge pressure gradient independently altered around the experimental value while keeping the total stored energy, total current and the plasma shape unchanged through adjusting the core profiles to incorporate the pedestal change. For each equilibrium on the grid, the growth rate for a spectrum of modes with different toroidal mode (n) numbers is evaluated using ELITE. The ELITE code is primarily designed for intermediate to high-n modes and has successfully predicted and improved the understanding of many features of the pedestal at the onset of ELMs. However, because ELITE uses an expansion assuming 1/n is small, it is not accurate at very low n (i.e. 1–3). Therefore, we scan the mode number n from 5 to 15 in the stability calculation presented. The peeling-ballooning stability map (figure 5) is obtained after 2475 ELITE stability calculations using 225 constructed model equilibria. The instability threshold is set to the value when the growth rate of the least

stable mode exceeds half of the ion diamagnetic frequency (ω_*) [39, 40], which is self-consistently varied with the pedestal pressure keeping the collisionality fixed. Along the low-n peeling mode boundary, the growth rate increases rapidly with the edge current density, for example, the growth rate increases by a factor of >100 with only 10% increase in the edge current density. The proximity of the operating point to the boundary indicates the stability of the plasma edge at the time selected. Consistent with the theory and previous stability analyses of some other QH plasmas with coherent EHO, the edge of this QH plasma is in the stable region, but very close to the low-n current density driven kink/peeling stability boundary.

Those profiles and kinetic equilibrium are then imported into the M3D-C1 code, which solves the resistive MHD fluid equations [18]. The modeling is conducted in full three-dimensional toroidal geometry, including plasma and the open field-line region inside the computational domain, and using an unstructured mesh with high-order elements to capture the diverted geometry. The SOL is closely connected to the pedestal and can have non-trivial effects on the edge stability. Therefore, the experimental profiles of the electron density, temperature, ion density, and pressure gradient in the SOL are also employed in the modeling. The experimental carbon ion temperature in the SOL is not used due to lack of equilibration with the SOL ions. While keeping the gradient the same as the experiment, the total pressure profile is set to a small value (usually a few percent of the total pressure on axis) but large enough that it is higher than the electron pressure in the SOL. The ion temperature in the SOL is then recalculated using the experimental ion density and the calculated ion pressure. This method also helps to avoid any sharp change in pressure profile, which can sometimes cause numerical errors. The M3D-C1 modeling results presented in this paper are carried out in linearized single fluid model with realistic transport parameters. The plasma resistivity (Spitzer model) and a resistive wall closely approximating the DIII-D vessel wall are implemented in the modeling. The M3D-C1 code is an initial-value code and evolves the solution in time according to the physical equations. In the linear calculation, the solution is a linear combination of a range of eigenmodes with the toroidal (n) mode number specified in each linear M3D-C1 run. After evolving the equations for sufficiently long time, the mode with the largest growth rate will dominate. Hence, for a given n, the code is run

until a single poloidal mode structure becomes dominant. Modeling is performed for input toroidal mode numbers from n = 1 to 7 for the QH plasma in figure 1 at t ~ 2420 ms.

3. Mode structure comparison between theory, experiments and modeling

The ELITE code has been one of the primary tools for building an understanding of the QH-mode [16,17]. Although a detailed benchmarking of the ELITE code and the M3D-C1 code (in the ideal MHD limit) has been made for ELMing discharges [41], here we compare the results from the two codes for the case of QH-mode with a strong EHO. In Figure 6, we compare the 2D eigenmode structure for n = 5 from the linear M3D-C1 modeling to that from the ELITE prediction. Although the rotational shear effect can be included in the ELITE calculation, ELITE does not include the effect of finite rotation magnitude, the fine structure of edge ExB rotation profile, or resistive wall effects, which M3D-C1 can include. With rotational effects are turned off, there is good agreement in the mode structures predicted by the two codes [figures 6(a-c)]. The M3D-C1 modeled mode exhibits a structure very similar to the kink/peeling mode predicted by ELITE. Applying the experimental rotation profile in the M3D-C1 modeling (more details in section III) results in the mode structures becoming poloidally elongated and radially tilted [figure 6(d)] similar to previous ELITE calculation of an n = 5 peeling-ballooning mode with rotation shear effect [8]. Since the M3D-C1 code is valid down to n = 1, it can be used to model strong EHO QH-modes cases which typically have dominant n = 1-3. As an example, the 2D eigenmode structure of an n = 1 mode from the M3D-C1 free-boundary modeling with the experimental rotation profile and the modeled resistive DIII-D vessel wall is shown in figure 6(e).

The magnetics synthetic diagnostic in the M3D-C1 code can return the predicted magnetic fluctuations on the machine wall, which can be compared to measurements of the magnetic poloidal sensor array [see figure 1(f)] for individual harmonics. Figure 7 shows such a comparison for the n=1 mode along the inner vessel wall on the high field side (HFS) and the outer vessel wall on the low field side (LFS). Each profile is plotted versus the distance from the machine midplane (z = 0) and a positive z value corresponds to a location above the midplane. The measurements show that the magnetic perturbation

at the midplane vessel wall is ~4 G, which corresponds to $\delta B/B \sim 2\times10^{-4}$. A least-squares fit was used to scale the predicted perturbation magnitude to the magnetics data. The predicted amplitude and unwrapped phase profiles along the outer and inner vessel wall agree with the measurements. The same comparison has also been made for the 2nd harmonic (n = 2) and reasonable agreement is found (figure 8).

Various internal fluctuation diagnostics detect the perturbations in the edge due to the EHO. For example, the temperature fluctuations associated with the EHO are observed on the edge ECE radiometer channels [figure 9(a)], but are absent on the core ECE radiometer channels [figure 9(b)]. In this discharge, BES and the newly installed MIR systems are tuned to measure the pedestal region. Clear signatures of the fundamental EHO along with several harmonics are detected on both instruments [figure 9(c) and (d)]. Note that the 5 Hz small and slow oscillations seen in some data are associated with the 5 Hz gapout sweeping as described in first paragraph of this section. By comparing the fluctuation measurements with the magnetics data both in time and in the frequency domain, the toroidal mode (n) number can be determined. The signal of each harmonic can be extracted to compare with the M3D-C1 modeling.

The similarity between the measured and modeled mode structure is evaluated by comparing the radial profile of measured edge temperature and density fluctuations to M3D-C1 modeling. Figure 10(a) is the 2D spectrogram of the edge temperature fluctuations at t ~ 2420 ms on the outer midplane measured by the ECE radiometer radial array. During the time window of interest, the emission of the edge ECE channels is optically thick, and the fundamental n=1, 9.75 kHz EHO and up to the 5th harmonic are resolved. The 2D spectrogram of the BES data is similar and exhibits strong edge density fluctuations due to the EHO. Good agreement is found in the comparison between the M3D-C1 modeling and the measurements, as can be seen in figure 10(b) for the temperature fluctuation of the fundamental n = 1 EHO and figure 10(c) for that of the 2nd harmonic. Both the modeled and the measured temperature fluctuations due to the EHO peak near R ~ 227 cm with full width at half maximum (FWHM) of ~2.5 cm radially extending over the entire pedestal region. Density fluctuations associated with the EHO with $\delta n/n$ up to 4% are detected on the edge BES channels and similar fluctuating density profiles are also found in the linear M3D-C1 modeling, as demonstrated in figure 10(d)

for the fundamental n=1 EHO. The slight radial broadening and inwards shift of the density fluctuation profile from the BES measurement relative to the modeling is partially due to the finite life time of the neutral beam atom excited state, the beam ion velocity and the finite spot size of the BES channels. Note that the predicted temperature or density perturbation eigenmode from the linear calculations is scaled using a least-squares fit to the experimental data, as also done for the comparison with the magnetics data.

The newly installed DIII-D MIR system also captures the fluctuations at the edge associated with the EHO. Localized density fluctuations in the vicinity of the cutoff layers modulate the local plasma index of refraction, which then impacts the reflected wave. When the optics are well-focused at the cutoff surface, the phase fluctuation of the reflected wave is proportional to the density fluctuation at the cutoff layer. Good optical coupling is achieved during the timeframe shown in figure 9(d) (concluded by examining the in-phase-quadrature (I/Q) plots), and features associated with the EHO from the fundamental n = 1 to the 7^{th} harmonic are observed and agree with those observed by other diagnostics in the time and frequency domains.

The correspondence between the phase modulation of the MIR signal and the density fluctuation due to the EHO is complicated. In order to make a truly "apples-to-apples" comparison, we apply the synthetic MIR diagnostic [42] using the full wave reflectometer code FWR2D [43] to calculate the reflectometer response (phase and magnitude) to the density fluctuations obtained by M3D-C1. This can then be directly compared with the measured MIR signal. A full-wave solution of the plasma-wave interaction is obtained in the vicinity of the cutoff layer. Effects of instrumental artifacts (e.g., misalignments) are also investigated using the synthetic MIR diagnostic and the results support the accuracy of the measurements. An example of the predicted 2D MIR phase signal using the prescribed M3D-C1 modeled n = 5 density fluctuations is presented in figure 11.

4. Comparison of wavelength

In addition, we compare the wavenumbers from the M3D-C1 modeling to the measurements, which is a more stringent test of the modeling. The poloidal wavenumber

can be inferred from the cross-phase of signals between two poloidally-separated channels divided by the separation. The poloidal wavenumbers of the fundamental EHO and several harmonics resolved from various diagnostics and from M3D-C1 modeling are summarized in Table 1. The MIR measured poloidal wavenumbers are quoted from the data shown in figure 12, which presents a spectral density representation of the experimental MIR data in frequency-wavenumber space. The 2D spectral density is generated by calculating the cross-phase between all poloidal pairs on a single cutoff surface at each frequency bin. An ensemble of cross-phase/frequency pairs are binned and averaged to generate the statistical representation [44] shown in figure 12. The poloidal wavenumbers of n = 1, 3, 5 modes inferred from FWR2D predictions using the same method are also listed in Table 1. The derived wavenumbers from FWR2D predicted MIR phase signal qualitatively agree with those from other diagnostics indicating the input M3D-C1 solution qualitatively represents the measured EHO.

Both BES and MIR measurements indicate that in the lab frame the coherent EHO rotates poloidally in the electron diamagnetic direction. It is worthwhile noticing in figure 12 that there are some broadband fluctuations at much lower amplitude propagating in the opposite direction. The weak broadband fluctuations are also observed on some other diagnostics, such as magnetic sensors and BES. QH plasmas with stronger and/or solely broadband fluctuations have also been observed [7]. Data from magnetic sensors, BES and MIR all suggest the toroidal rotation direction of the coherent EHO follows the plasma rotation, whereas the broadband fluctuations follow the plasma current direction instead. Therefore, with counter-Ip NBI, like the situation in discharge 157102, the coherent EHO and the broadband fluctuations have poloidal wavenumbers with opposite sign. Consequently, the inferred wavenumber of the coherent EHO from measurements can be slightly underestimated due to the influence of the background broadband fluctuations. Nevertheless, general agreement is found between the M3D-C1 modeling and the measurements. The poloidal wavenumber increases with the toroidal mode number indicating these harmonics share nearly the same phase velocity.

Table 1: poloidal wavenumber (cm^{-1}) of EHO

k_{pol}	n=1	n=2	n=3	n=4	n=5	n=6	n=7

M3D-C1 (±0.04)	0.03	0.04	0.06	0.09	0.12	0.14	0.18
Magnetics (±0.03)	0.02	0.04	0.06				
BES (±0.02)	0.02	0.03	0.04	0.04	0.05		
FWR2D (±0.01)	0.03		0.06		0.12		
MIR (±0.06)	0.02	0.03	0.05	0.07	0.10	0.13	0.09
ECE-I (±0.1)	0.03	0.05					

III. Rotation and Rotational Shear Effects on EHO

While previous current ramp experiments [7, 12] and recent non-linear modeling of EHO [45] have shown the importance of edge current density in driving the EHO, The EHO is destabilized at edge current densities below those required to trigger low-n current density driven ELMs. Experiments and theories suggest that the rotational shear as additional drive of the coherent EHO. The QH-mode operation has been successfully accessed on many devices, first on DIII-D [4,5], and subsequently on ASDEX-U [14,46], JET [14], and JT-60U [47, 48]. In all these cases, the QH-mode plasma with the coherent EHO was created with strong plasma rotation and rotational shear in the pedestal region. Comparison with peeling-ballooning mode stability calculations indicates that QH-mode is operating near, but somewhat below, the peeling boundary computed without rotation, while the toroidal rotational shear is destabilizing for the low n modes in this region. This suggests that the EHO is a rotationally destabilized saturated low-n current-driven kink/peeling mode. Initial experimental data and analysis [13, 15] suggest the shear in the toroidal rotation associated with the ExB drift is a more important parameter than the shear in the toroidal fluid rotation used in the model of EHO based on single fluid ideal MHD theory [8]. Here, we extend the previous work by investigating the influence of the edge toroidal ExB rotational shear, and the resistive wall on the linear growth rate of modes down to n=1-3 as commonly observed for strong EHOs via M3D-C1 linear calculations.

The role of edge toroidal ExB rotational shear is studied with discharge 153440. In this discharge ($|B_T| \sim 1.91$ T, $|I_p| \sim 1.5$ MA, B_T and I_p in the same direction, slightly biased to lower single null shape, $\kappa \sim 1.85$, $\delta \sim 0.5$, gapout ~ 11 cm, gapin ~ 4.5 cm,

dRsep ~ -1 cm), the QH-mode begins around t = 1590 ms as indicated by the D-alpha signal [figure 13(a)]. A coherent EHO with dominant n = 2 component appears at the same time and lasts to t ~ 1820 ms [figure 13(b)], which provides continuous transport and maintains the constant density [figure 13(c) and (d)]. The plasma rotates in the counter-Ip direction with strong and constant counter-Ip torque from NBI. Notice that the edge rotation decreases when the coherent EHO switches on and increases again after the end of the coherent EHO phase (~1830 ms) [figure 13(e)]. The decrease in plasma rotation and rotational shear is a feature of the coherent EHO commonly observed in the experiments, indicative of momentum transport from the EHO that may be involved in the saturation mechanism [8]. Pedestal profile analyses, peeling-ballooning stability calculations and M3D-C1 modelings were carried out around t = 1725 ms.

The stability calculation for this discharge at the analyzed time [figure 14] indicates again that the plasma is marginally stable to the kink/peeling boundary without rotation. The stability boundary is calculated using ELITE code including the ion diamagnetic effects but not the rotational shear effects. The MHD stability threshold formulated in this way has been shown to be in agreement with the ELM and EHO onset conditions for a wide range of tokamaks and experimental conditions. Statistically, the QH plasma edge with coherent EHOs is lower than the kink/peeling boundary computed without rotation while the plasma edge with ELMs following the cessation of the EHOs is at that boundary. The analyzed operational point shown in figure 14 is slightly below the kink/peeling instability threshold and n=10 is the least stable mode.

A series of M3D-C1 runs with different plasma rotation profiles were conducted to assess the influence of rotation and rotational shear. The rotation velocity input into M3D-C1 is $V_{M3D-C1} = R^2\omega_{M3D-C1}(\psi)\nabla\phi$ in the toroidal direction. In the single fluid modeling, there is no distinction between the electron and ion drift velocity perpendicular to the magnetic field and the *E*x*B* drift, that is, $\omega_{M3D-C1} = \omega_E = \omega_i = \omega_e$ are used, where $\omega_E = \frac{E_r}{|RB_P|}$ is the toroidal angular velocity associated with the *E*x*B* drift. Here, the *E*x*B* shear ($\omega_{E\times B}$) is the shear in ω_E.

$$\omega_{E\times B} = \frac{(RB_P)^2}{B}\frac{\partial\omega_E}{\partial\psi}$$

Initial experimental data show that a large shear in ω_E is conserved in QH-mode plasmas under various conditions. This suggests that ω_E might be the fundamental rotation velocity and $\omega_{E\times B}$ might be the critical shear for creating and sustaining the QH-mode or the coherent EHO [13, 15]. Accordingly, we choose the magnitude of ω_E from experiments as ω_{M3D-C1} in these single fluid modelings.

In experiments, the ω_E is calculated from the measurements of carbon ions (the main impurity on DIII-D). The CER system on DIII-D has 64 spatial views, 48 viewing tangentially, and 24 viewing vertically. CER provides the rotation measurement, typically of the carbon impurity ion rotation, using lines radiated by charge exchange between neutrals in the neutral beams and the fully stripped carbon ions, which exist everywhere in the discharge. The *E*x*B* rotation angular velocity is obtained from the toroidal rotation velocity (V_T), poloidal rotation velocity (V_P), the density (n_c), and temperature (pressure P_c) of carbon measured by CER,

$$\omega_E = \omega_{*c} - \omega_{V\times B}$$

where $\omega_{V\times B} = \frac{V_T}{R} - \frac{V_P B_T}{|RB_P|}$ is the v×B rotation angular velocity for carbon, and $\omega_{*c} = \nabla P_c / 6n_c$ is the carbon diamagnetic rotation angular velocity. The experimental measurement and the fit of the carbon toroidal, poloidal, v×B, diamagnetic rotation angular velocity profiles at the time selected are shown in figure 15 for the outer radial region, along with the calculated *E*x*B* rotation angular velocity profile. It is worthy noticing that in the pedestal where the EHO lives, there are differences between the ExB rotation and the toroidal rotation.

In this modeling series, all the other inputs are identical except for the rotation (ω_E), which is scanned from 0 to 100% of the experimental value through four incremental steps [figure 16(a)]. The rotational shear ($\partial\omega_E/\partial\psi$) is computed self-consistently from ω_E. M3D-C1 runs for n=1 to n=10 are then made for each of these rotation profiles. The linear growth rates of all these modes in the rotation scan are plotted in figure 16(b). Stabilization by rotation and/or rotational shear occurs for all the modes with n≥3. The growth rates of n=1 is almost unchanged by rotation. Interestingly, rotation and/or rotational shear destabilizes the n=2 mode. This is in agreement with the experiment where a dominant n=2 EHO is detected in this QH plasma [figure 13(b)] and in line with the general experimental observations of coherent EHO disappearing and ELMs

appearing when the edge rotation is reduced. Those ELMs that follow the cessation of coherent EHOs have higher mode n number (typically n≥ 5~6) and an operating point statically shown to be at the low-n current density driven peeling stability boundary computed without rotation, while QH-mode with the coherent EHO is further from that stability boundary [10]. This is also consistent with the theory of the EHO being a rotational shear destabilized kink/peeling mode. However, the rotational shear effect and possible finite rotation effect are not de-coupled in this series of modelings and non-linear simulation is desirable to explore how the mode manifests after growing into a larger size and how it saturates.

The peeling-ballooning theory predicts the QH-mode can exist with both signs of rotation as long as the edge rotational shear is large. Although the QH-mode is more readily created with counter-Ip NB injection, it also has been obtained with co-Ip NB injection on DIII-D [11]. This result has been reproduced in the M3D-C1 modeling of the same discharge 153440 utilizing a rotation profile with reversed sign, that is, flipped from experimental counter-Ip rotation to co-Ip rotation while the absolute amplitude is kept the same. The calculated linear growth rate of the n=2 mode in co-rotation is only 2% lower than in counter-rotation. This small difference is mainly due to the fact that the plasma resistivity is included in the M3D-C1 modeling. For ideal MHD, the growth rate is invariant under the reversal of the equilibrium rotation velocity. However, if other non-ideal effects, such as the plasma resistivity, are included, the growth rate is not expected to be exactly the same under the reversal of the plasma rotation alone.

M3D-C1 results presented so far are all from modeling with a resistive wall. Comparing to modeling with an "ideal" wall (a wall with resistivity of 10^{-6}), the growth rate calculated with a resistive wall is higher. However, the rotation and/or rotational shear has a bigger effect on the growth rate, for example, the growth rate of the n=2 in discharge 153440 computed with rotation and an "ideal" wall is about four times larger than that computed with resistive wall but without rotation.

IV. Summary and Discussion

QH-mode is a promising alternative operating mode without ELMs that has been achieved on many magnetic confinement fusion devices. The coherent EHO is a key

feature of most QH-modes for providing a continuous transport channel that maintains the pedestal just below the ELM stability boundary. Experimentally, the formation of EHO requires strong edge rotation and rotational shear. To better understand the EHO physics and the role of rotational shear, and to extend the QH-mode operating region, this paper presents the numerical investigation using the M3D-C1 code which allows modeling low, experimentally relevant, toroidal mode numbers and includes the effects of ExB rotational shear and the resistive wall. Indeed, we find the destabilization effects of rotational shear on low-n EHO-like modes in the modeling.

The modeled mode structure from these linear M3D-C1 calculations agrees qualitatively with the low-n kink/peeling mode predicted by the ideal MHD ELITE code and with the measurements of the coherent EHO from various diagnostics [edge magnetics sensors, ECE, BES, ECE-Imaging, and microwave imaging reflectometer (MIR)]. The wavenumbers of the modeled modes are also consistent with the measurements. Similar to the measured EHO, the modeled mode extends over the edge pedestal (FWHM~2.5 cm) while the amplitude peaks in the edge steep gradient region; the poloidal wavenumber increases with the toroidal mode number, from ~0.02 cm^{-1} for n=1 to ~0.2 cm^{-1} for n=7. To our knowledge, this is the most comprehensive direct comparison of modeling with measurements of the EHO mode structure to date. These similarities demonstrate the validity of applying the M3D-C1 code to numerically study the EHO.

In a series of linear calculations using the M3D-C1 code to model QH plasmas with various ExB rotation profiles, we find that the rotation and/or rotational shear destabilizes the n=2 mode while stabilizing high-n modes. The different effects on low-n and high-n modes are consistent with the experimental observations of the loss of low-n coherent EHO and the appearance of higher-n ELMs at too low edge rotation. This is also in line with previous results that the operating point of QH-mode with coherent EHOs is statistically further from the peeling mode stability boundary computed without rotation than ELMing H-mode. M3D-C1 predicts that n=2 is the most unstable mode at the experimental rotation level, consistent with the dominant EHO mode observed in the experiment. The calculated growth rate is nearly unchanged (only 2% lower) under reversal of the plasma rotation, which is consistent with the theory and previous

experimental observations indicating the independence of EHO on the rotation direction. These findings again support the theoretical prediction of ExB rotational shear effects on EHO and indicate ExB rotational shear being an important parameter for generating and sustaining EHO. However, the rotation and rotational shear variation are not de-coupled in these modelings. Future work will try to investigate the possible finite rotation effect on the EHO.

The inclusion of the diamagnetic effect in the M3D-C1 full two-fluid model results in different values for ω_i, ω_e and ExB rotation frequency, $\omega_{\mathrm{i}} = \omega_{*\mathrm{i}} + \omega_{\mathrm{ExB}}$ and $\omega_{\mathrm{e}} = \omega_{*\mathrm{e}} + \omega_{\mathrm{ExB}}$ where $\omega*$ is the diamagnetic frequency; therefore, two-fluid modeling is underway and will try to distinguish the impact that each of these have on the EHO. The two-fluid modeling results may help to identify which component of rotation is the most important for obtaining QH-mode and help to understand the differences between co- and counter-injection.

Non-linear effects also can be important especially in regard to the EHO saturation as shown by QH-mode simulations [45,49] using the JOREK code. In principle, non-linear simulation can be performed using the M3D-C1 code; however, nonlinear calculations using experimentally relevant parameters and with sufficient resolution to reproduce ideal peeling-ballooning growth rates are presently extremely computationally expensive, and have not yet been attempted. Furthermore, transport processes that are suspected to play a role in the EHO saturation, such as the modification of the edge rotation and density profile by the EHO, are likely due to turbulent or neoclassical effects not yet present in the M3D-C1 model. Still, nonlinear modeling in the absence of these processes would be instructive, and nonlinear modeling with M3D-C1 using reduced models, or with fully compressible models and anomalous diffusion, will be pursued in the near future to explore the nonlinear development of these modes.

Acknowledgments

This material is based upon work supported by the U.S. Department of Energy, Office of Science, Office of Fusion Energy Sciences, using the DIII-D National Fusion Facility, a DOE Office of Science user facility, under Awards DE-FC02-04ER54698, DE-FG03-97ER54415, DE-AC02-09CH11466, DE-FG02-99ER54531, and DE-FG02-08ER54999. DIII-D data shown in this paper can be obtained in digital format by following the links at https://fusion.gat.com/global/D3D_DMP. The author (XC) would like to thank Ted Strait, Carlos Paz-Soldan, Craig Petty, Gustavo Canal, Yan Zhao, Ming Chen, and the DIII-D team.

References

[1] A.W. Leonard et al., Phys. Plasmas 21, 090501 (2001).
[2] A. Loarte et al., Progress in the ITER Physics Basis Chapter 4: Power and particle control 2007 Nucl. Fusion 47 S203
[3] ITER Physics Basis Editors ,et al. 1999 Nucl. Fusion 39 2137
[4] K. H. Burrell et al., Phys. Plasmas 8, 2153 (2001).
[5] C.M. Greenfield, et al., Phys. Rev. Lett. 86, 4544 (2001).
[6] B.A. Grierson, et al., Phys. Plasmas 22, 055901 (2015).
[7] K.H. Burrell, et al., Phys. Plasmas 12, 056121 (2005).
[8] P.B. Snyder, et al., Nucl. Fusion 47, 961 (2007).
[9] T.H. Osborne, et al., J. of Phys. 123, 012014 (2008).
[10] K.H. Burrell, et al., Nucl. Fusion 49, 085024 (2009).
[11] K.H. Burrell, et al., Phys. Rev. Lett. 102, 155003 (2009).
[12] W.P. West, et al., Nucl. Fusion 45, 1708 (2005).
[13] K.H. Burrell, et al., Phys. Plasmas 19, 056117 (2012).
[14] W. Suttrop, et al., Nucl. Fusion 45, 721 (2005).
[15] A.M. Garofalo, et al., Nucl. Fusion 51, 083018 (2011).
[16] P.B. Snyder, H.R. Wilson, et al., Phys. Plasmas 9, 2037 (2002).
[17] H.R. Wilson, P.B. Snyder, R.L. Miller, and G.T.A. Huysmans, Phys. Plasmas 9, 1277 (2002).
[18] N.M. Ferraro, S.C. Jardin, J. Comput. Phys. 228, 7742 (2009).
[19] N. Aiba, et al., Nucl. Fusion 50, 045002 (2010).
[20] W.M. Solomon, et al., Phys. Rev. Lett. 113, 135001 (2014).
[21] D. M. Ponce-Marquez, et al., Rev. Sci. Instrum. 81, 10D525 (2010).
[22] R. P. Seraydarian, K. H. Burrell, and R. J. Groebner, Rev. Sci. Instrum. 59, 1530 (1988).
[23] R. J. Groebner, K. H. Burrell, and R. P. Seraydarian, Phys. Rev. Lett. 64, 3015 (1990).
[24] M.E. Austin and J. Lohr, Rev. Sci. Instrum. 74, 1457 (2003).
[25] E.J. Strait, Rev. Sci. Instrum. 77, 023502 (2006).
[26] B.J. Tobias, et al., Rev. Sci. Instrum. 83, 10E329 (2012).

[27] G. McKee, et al., Rev. Sci. Instrum. 70, 913 (1999).
[28] C.M. Muscatello, et al., Rev. Sci. Instrum. 85, 11D702 (2014).
[29] T. Osborne's Python-based data Analysis Toolkit. https://diii-d.gat.com/diii-d/PyD3D
[30] L.L. Lao, H. St John, R.D. Stambaugh, A.G. Kellman and W. Pfeiffer, Nucl. Fusion 25, 1611 (1985)
[31] R.J. Groebner, et al., Nucl. Fusion 41, 1789 (2001).
[32] Stangeby, P. C., *The plasma boundary of magnetic fusion devices*. (Institute of Physics Pub., Bristol ; Philadelphia, 2000).
[33] R.J. Goldston, et al., J. Comp. Phys. 43, 61 (1981).
[34] A. Pankin, et al., Comp. Phys. Commu. 159, 157 (2004).
[35] St. John H., Taylor T.S., Lin-Liu Y.R. and Turnbull A.D. 1994 Transport simulation of negative magnetic shear discharges Proc. 15th Int. Conf. on Plasma Physics and Controlled Nuclear Fusion Research (Seville, Spain) p 603 (naweb.iaea.org/napc/physics/FEC/STIPUB948 VOL3.pdf)
[36] C.T. Holcomb, et al., RSI 77, 10E506 (2006).
[37] O. Sauter, C. Angioni and Y.R. Lin-Liu, Phys. Plasmas 6, 2834 (1999).
[38] O. Sauter, C. Angioni and Y.R. Lin-Liu, Phys. Plasmas 9, 5140 (2002).
[39] K.V. Roberts K.V. and J.B. Taylor, Phys. Rev. Lett. 8, 197 (1962).
[40] Tang W.M. et al Nucl. Fusion 22 1079 (1982).
[41] N.M. Ferraro, et al., Phys. Plasmas 17, 102508 (2010).
[42] X. Ren, et al., 1st EPS conference on Plasma Diagnostics paper, Journal of Instrumentation, Vol. 10, (2015) http://dx.doi.org/10.1088/1748-0221/10/10/P10036
[43] G.J. Kramer et al, Plasma Phys. Control. Fusion, 46, 695 (2004).
[44] J. M. Beall, Y. C. Kim, and E. J. Powers, J. Appl. Phys. 53, 3933 (1982).
[45] W. Suttrop, et al., Plasma Phys. Controlled Fusion 45, 1399 (2003).
[46] Y. Sakamoto, et al., Plasma Phys. Controlled Fusion 46, A299 (2004).
[47] N. Oyama, et al., Nucl. Fusion 45, 871 (2005).
[48] F. Liu, et al., Nucl. Fusion 55 (2015) 113002
[49] A.M. Garofalo, et al., Phys. Plasmas 22, 056116 (2015).

Figure Captions

Figure 1: Time evolution of several plasma parameters (discharge 157102): (a) total injected NBI power and total radiated power, (b) average line-integrated density, (c) pedestal density, (d) Fourier analysis of signals from edge toroidal array of magnetic sensors, the toroidal (n) mode number of the modes labeled on the right, positive n number means the mode rotates in the neutral beam injection direction, (e) the intensity of the Dα light measured by a filterscope viewing the lower divertor, (f) the distance between the last close flux surface and the vessel wall at the outer midplane.

Figure 2: (color online) Plasma poloidal cross-section of typical highly shaped QH plasma discussed in this paper overlaid with several diagnostics that provide important measurements for this study: blue dots --- TS, red crosses --- CER, magenta shaded region (cartoon drawing for illustration, the size is not accurate) --- MIR/ECE-I viewing window, green rectangular region --- the 2D coverage area measured by BES. Insets show expanded views of 64 BES channels and the edge channels of TS and CER. There is also a 40-channel ECE system along the midplane from core to SOL [not shown].

Figure 3: (color online) Discharge 157102, full radial profiles of several key plasma parameters fitted using data [symbols in red] from various diagnostics. X-axis is the normalized poloidal flux. (a) Electron density (n_e) and (b) temperature (T_e) data are obtained from TS, (c) The electron pressure is the product of n_e and T_e, (d) impurity (carbon) density (n_c), (e) ion temperature (T_i), and (f) carbon toroidal/poloidal rotation (V_{tor}/V_{pol}) are obtained from CER along with the calculated toroidal rotation associated with ExB drift (V_{ExB}). Note that $V_{ExB} = R\omega_E$. Ion density can be calculated by $n_i=n_e-6n_c$, assuming carbon is the sole impurity.

Figure 4: (color online) Discharge 157102, pedestal profiles of several key plasma parameters fitted using data with error bars [symbols in red] from various diagnostics: Pedestal profile of (a) electron density (n_e), (b) electron temperature (T_e), (c) electron pressure is the product of n_e and T_e, (d) impurity (carbon) density (n_c), (e) ion temperature (T_i), (f) toroidal/poloidal rotation (V_{tor}/V_{pol}) and calculated V_{ExB}. (g) input experimental (red) and final (after iterations) kinetic (black) total pressure, (h) normalized experimental (red) and final kinetic (black) current density (j_N); and contributions from Ohmic current density (j_{OH}) (blue), Bootstrap current density (j_{BS}) (green) and NBI driven current density (j_{NBI}) (cyan)

Figure 5: (color online) Peeling-ballooning stability analysis at 2420ms in discharge 157102: The contour plot of the ratio of the growth rate (g) of least stable mode calculated using ELITE to half of the ion diamagnetic frequency (ω_*) at a set equilibria varying around the experimental kinetic equilibrium. Horizontal axis is the peak values of normalized pedestal pressure gradient (α) and vertical axis is half of the peak edge current normalized by the volume averaged current density. The blue region is stable ($\gamma/(\omega_*/2) < 1$), the red region is unstable ($\gamma/(\omega_*/2) > 1$), and the white solid line is the instability boundary ($\gamma/(\omega_*/2) = 1$). The close proximity of the operational point

(open square with typical uncertainty) to the low-n kink/peeling stability boundary is consistent with the theory and previous experiments.

Figure 6: (color online) Good agreement between (a) the displacement of n=5 mode from ELITE prediction and (b) pressure fluctuations due to n=5 from M3D-C1 linear simulation without rotation, (c) is close-up look of the region near the outer midplane. (d) sheared mode structures seen in M3D-C1 modeling with experimental rotation. The pink solid line is the last closed flux surface. (e) Pressure fluctuations due to n=1 from M3D-C1 linear calculation with rotation. The green solid line indicates the modeled resistive DIII-D vessel wall. All at 2420ms in discharge 157102 but at arbitrary toroidal angles.

Figure 7: (color online) Reasonable agreement in (a) the mode structure on low field side, (b) the mode structure on high field side (red) and (c) unwrapped phase on LFS, HFS (red) of magnetic fluctuations due to fundamental n=1 from poloidal magnetic sensors data (open triangular or square) and M3D-C1 linear calculation (solid line) at 2420ms in discharge 157102. Those are plotted versus the distance along the vessel wall, z=0 is at the machine midplane, positive z means above the midplane. Note in (a) and (b), M3D-C1 prediction is scaled by least-squares fit to the magnetics data.

Figure 8: (color online) Reasonable agreement in (a) the mode structure on low field side, (b) the mode structure on high field side (red) and (c) unwrapped phase on LFS, HFS (red) of magnetic fluctuations due to n=2 from magnetic measurements (open triangular or square) and M3D-C1 linear calculation (solid line) at 2420ms in discharge 157102. Same as figure 7, those are plotted versus the distance along the vessel wall, and M3D-C1 predicted magnitude in (a) and (b) are scaled by least-squares fit to the magnetics data.

Figure 9: (color online) Discharge 157102. Windowed power spectrum of ECE radiometer data at (a) the pedestal and (b) the core. Windowed power spectrum of (c) BES and (d) MIR data in the pedestal region.

Figure 10: (color online) Discharge 157102 near 2420ms. (a) power spectrogram of the ECE radiometer data where the strong temperature fluctuations at 9.75 kHz is due to the fundamental n=1 EHO, the strong signal at 19.5 kHz is associated with the 2^{nd} harmonic, etc; the power spectrogram of the density fluctuations detected by BES is quite similar; comparison of the radial profile of the (b) fundamental n=1 EHO and (c) 2^{nd} harmonic from ECE measurement (black) and M3D-C1 modeling (red); the horizontal bar represents the emissive layer (the 90% power width) for each ECE channel; (d) comparison of the radial profile of density fluctuations due to the fundamental n=1 EHO from BES measurement (uncertainties are also shown) and M3D-C1 modeling (red). M3D-C1 predictions are scaled by least-squares fit to the ECE or BES data. The temperature and density profiles are scaled and plotted in dashed line in (b)-(c) to illustrate the mode location related to the pedestal.

Figure 11: (color online) (a) Density fluctuations associated with 5th harmonic of the EHO modeled by M3D-C1 near 2420ms in discharge 157102 are input into the synthetic

MIR diagnostic to generate (b) the phase fluctuations that would be detected by the MIR diagnostic. The series of panels represent a time sequence. (c) The statistically resolved wavenumber of the n=5 mode is ~0.12cm^{-1}

Figure 12: (color online) Power spectral density measured by a MIR channel at Ψ_N ~ 0.92 near 2420ms in discharge 157102. It is plotted versus frequency (y-axis) and poloidal wavenumber (x-axis). The dashed lines are guides to the eye.

Figure 13: (color online) Time evolution of several plasma parameters (discharge 153440): (a) the intensity of the Dα light as an indicator of ELMs, (b) magnitude of modes measured by edge magnetics sensors, dominated by n=2 (c) Fourier analysis of magnetics senor data, color codes following the toroidal mode numbers, positive n number means rotates in the NBI direction, (d) line-integrated density (black) and pedestal density (blue), (e) normalized beta, and (f) edge (Ψ_N ~ 0.95) rotation measured by CER.

Figure 14: (color online) Peeling-ballooning stability analysis at 1725ms in discharge 153440

Figure 15: (color online) Toroidal (blue: open squares are measurements with error bars, solid line is the fit), poloidal (red: open squares are measurements with error bars, solid line is the fit), vxB (green), diamagnetic (ω_{*c}) (magenta) and ExB (black) angular rotation profiles of carbon ions at t=1725ms in discharge 153440.

Figure 16: (color online) (a) Rotation profile is scanned in the modeling in step of 25% of the experimental inferred value, (b) the linear growth rates of modes from n=1 to 10 returned in this series modeling.

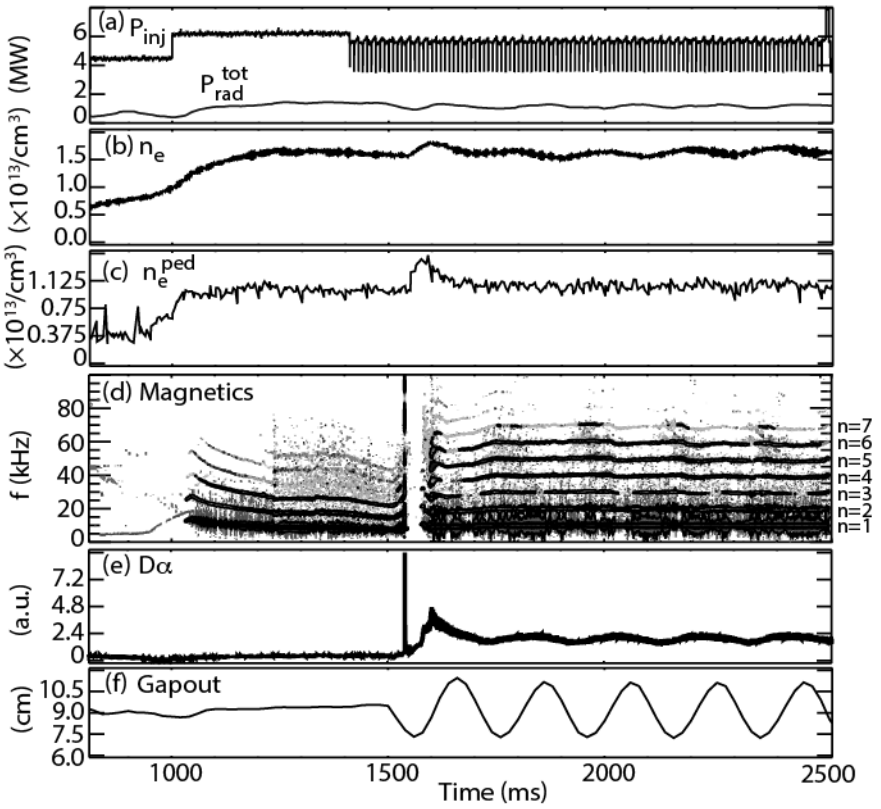
(a) P_{inj}
P_{rad}^{tot}
(MW)
(b) n_e
$(\times 10^{13}/cm^3)$
(c) n_e^{ped}
$(\times 10^{13}/cm^3)$
(d) Magnetics
f (kHz)
n=7
n=6
n=5
n=4
n=3
n=2
n=1
(e) Dα
(a.u.)
(f) Gapout
(cm)
1000
1500
2000
2500
Time (ms)

Chen Fig. 1

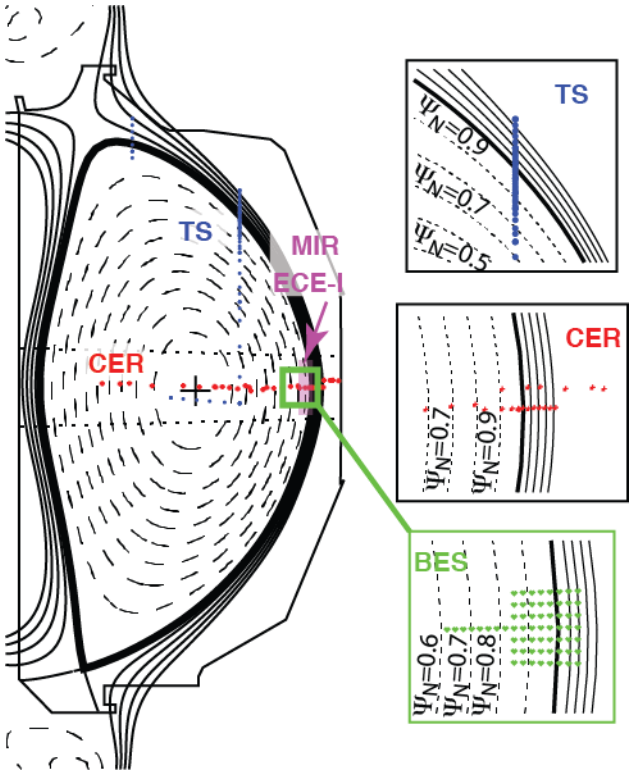
TS
MIR
ECE-I
CER
TS
Ψ_N=0.9
Ψ_N=0.7
Ψ_N=0.5
CER
Ψ_N=0.7
Ψ_N=0.9
BES
Ψ_N=0.6
Ψ_N=0.7
Ψ_N=0.8

Chen Fig. 2

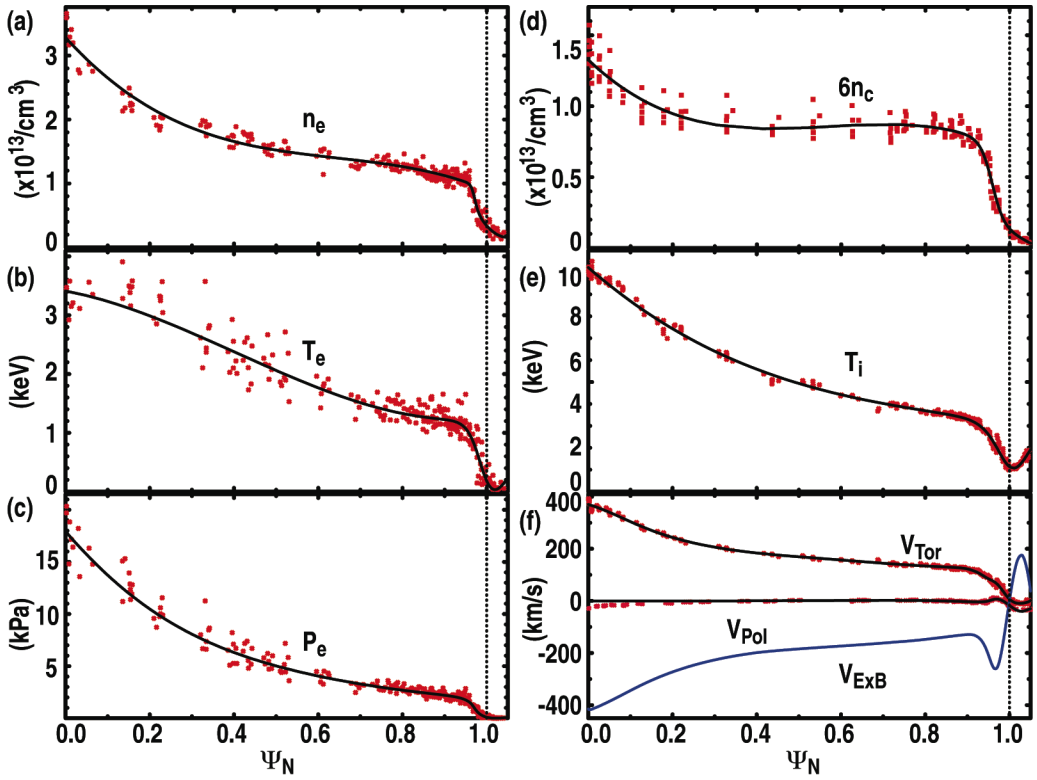
(a)
(x10^13/cm^3)
n_e
(b)
(keV)
T_e
(c)
(kPa)
P_e
Ψ_N
(d)
(x10^13/cm^3)
6n_c
(e)
(keV)
T_i
(f)
(km/s)
V_Tor
V_Pol
V_ExB
Ψ_N

Chen Fig. 3

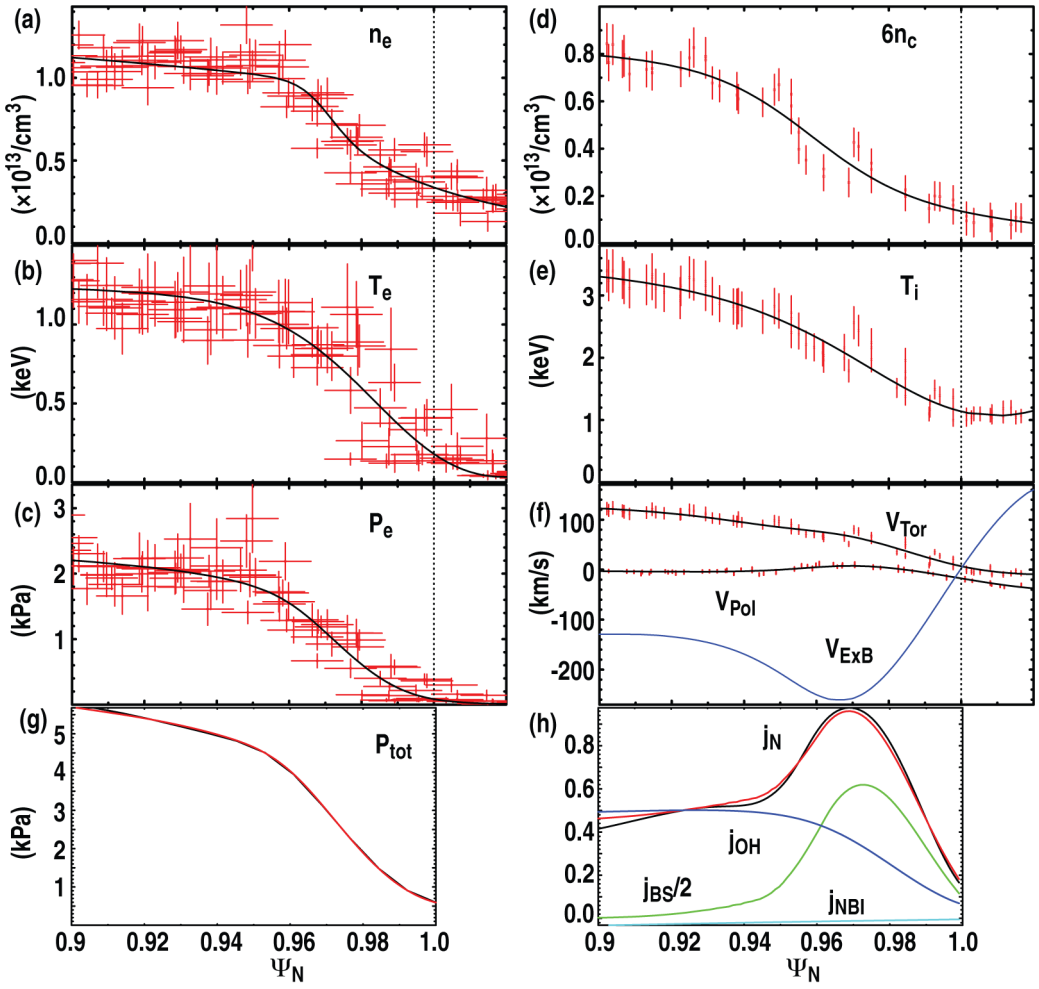
(a)
n_e
$(\times 10^{13}/cm^3)$
(b)
T_e
(keV)
(c)
P_e
(kPa)
(g)
P_{tot}
(kPa)
Ψ_N
(d)
$6n_c$
$(\times 10^{13}/cm^3)$
(e)
T_i
(keV)
(f)
V_{Tor}
V_{Pol}
V_{ExB}
(km/s)
(h)
j_N
j_{OH}
$j_{BS}/2$
j_{NBI}
Ψ_N

Chen Fig. 4

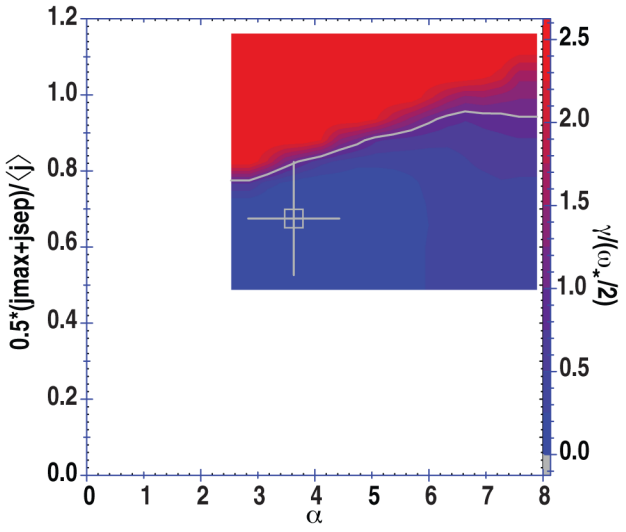
1.2
1.0
0.8
0.6
0.4
0.2
0.0
0.5*(jmax+jsep)/⟨j⟩
0
1
2
3
4
5
6
7
8
α
2.5
2.0
1.5
1.0
0.5
0.0
γ/(ω*/Z)

Chen Fig. 5

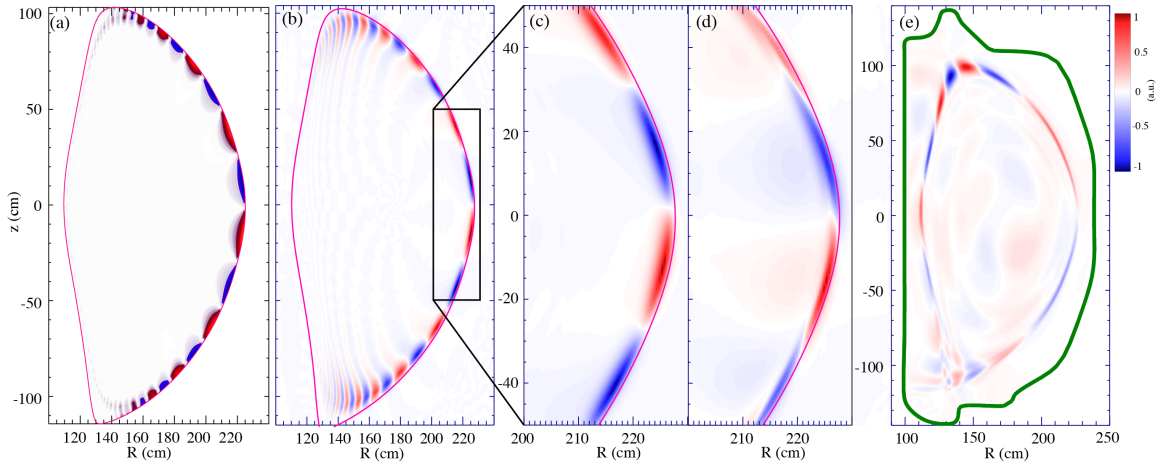

Chen Fig. 6

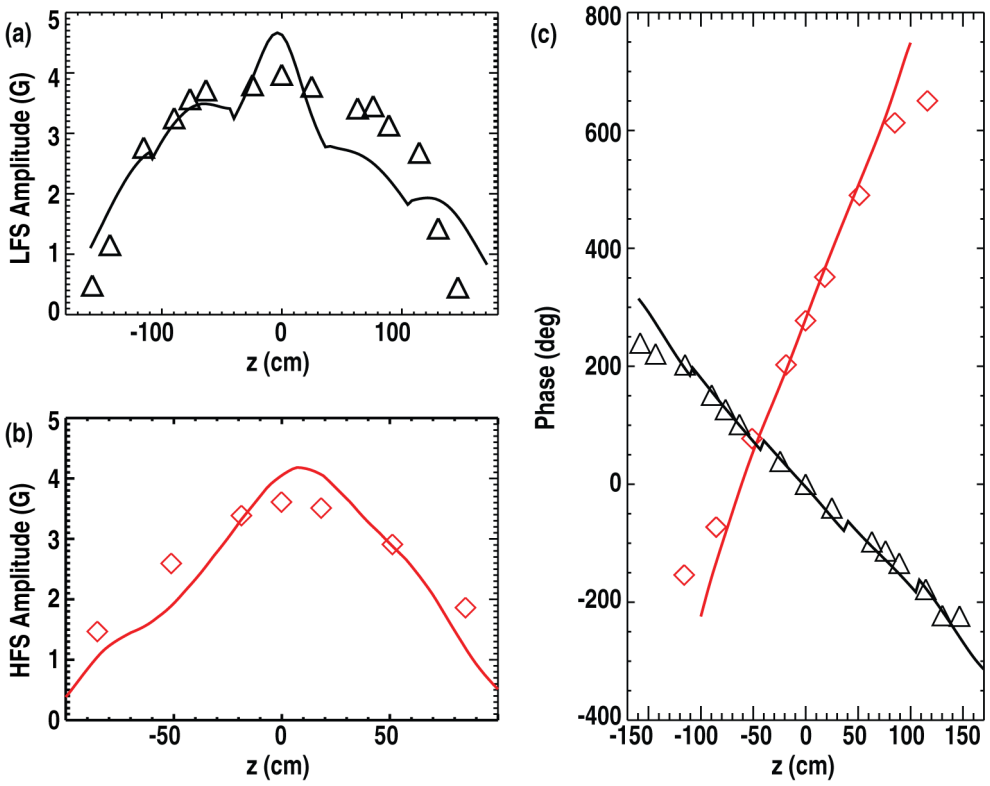

Chen Fig. 7

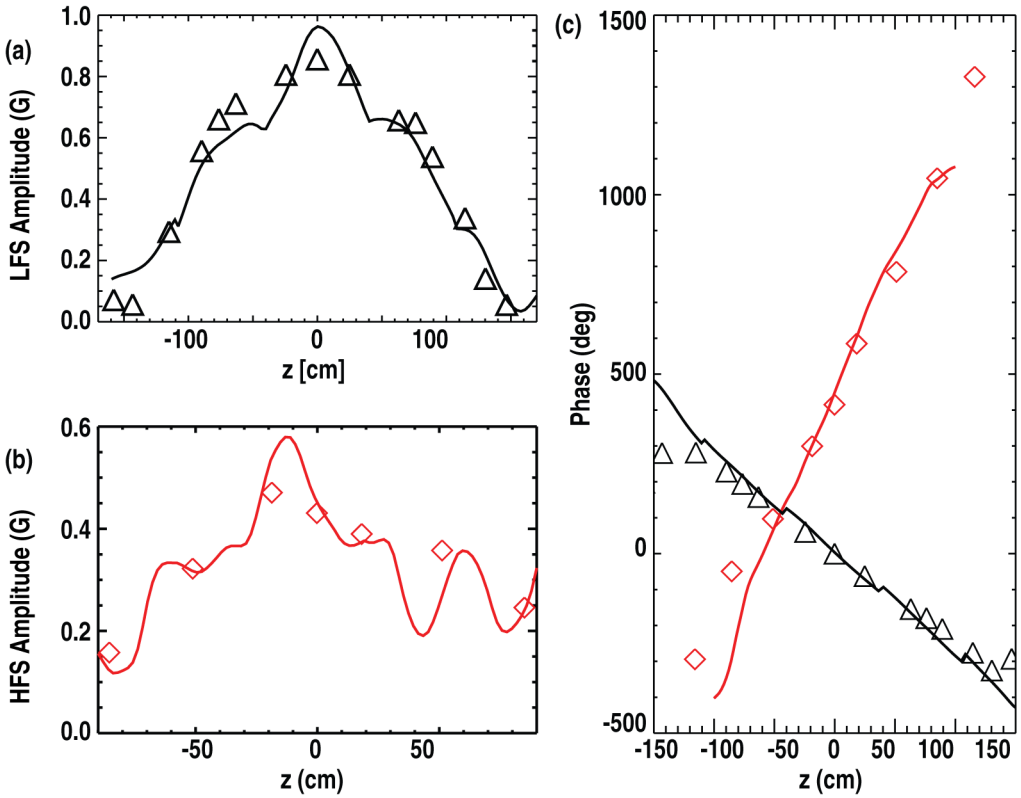
(a)
LFS Amplitude (G)
1.0
0.8
0.6
0.4
0.2
0.0
-100
0
100
z [cm]
(b)
HFS Amplitude (G)
0.6
0.4
0.2
0.0
-50
0
50
z (cm)
(c)
Phase (deg)
1500
1000
500
0
-500
-150
-100
-50
0
50
100
150
z (cm)

Chen Fig. 8

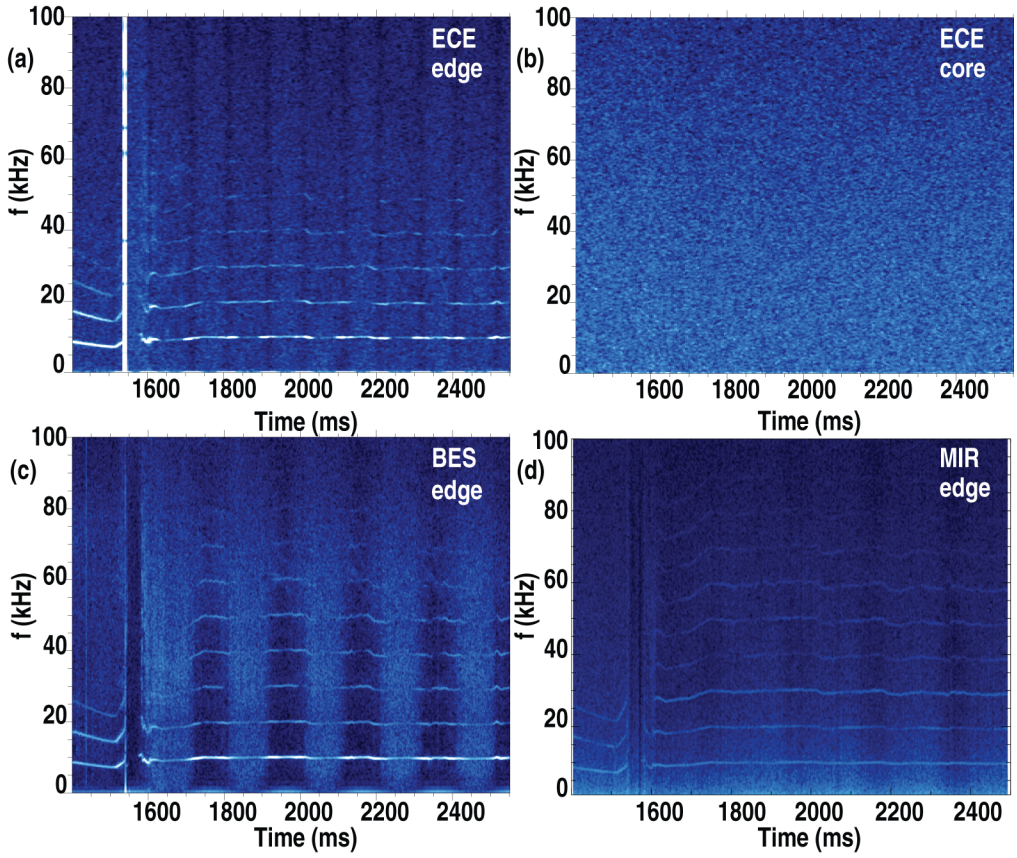
(a)
ECE
edge
(b)
ECE
core
(c)
BES
edge
(d)
MIR
edge
f (kHz)
Time (ms)
0
20
40
60
80
100
1600
1800
2000
2200
2400

Chen Fig. 9

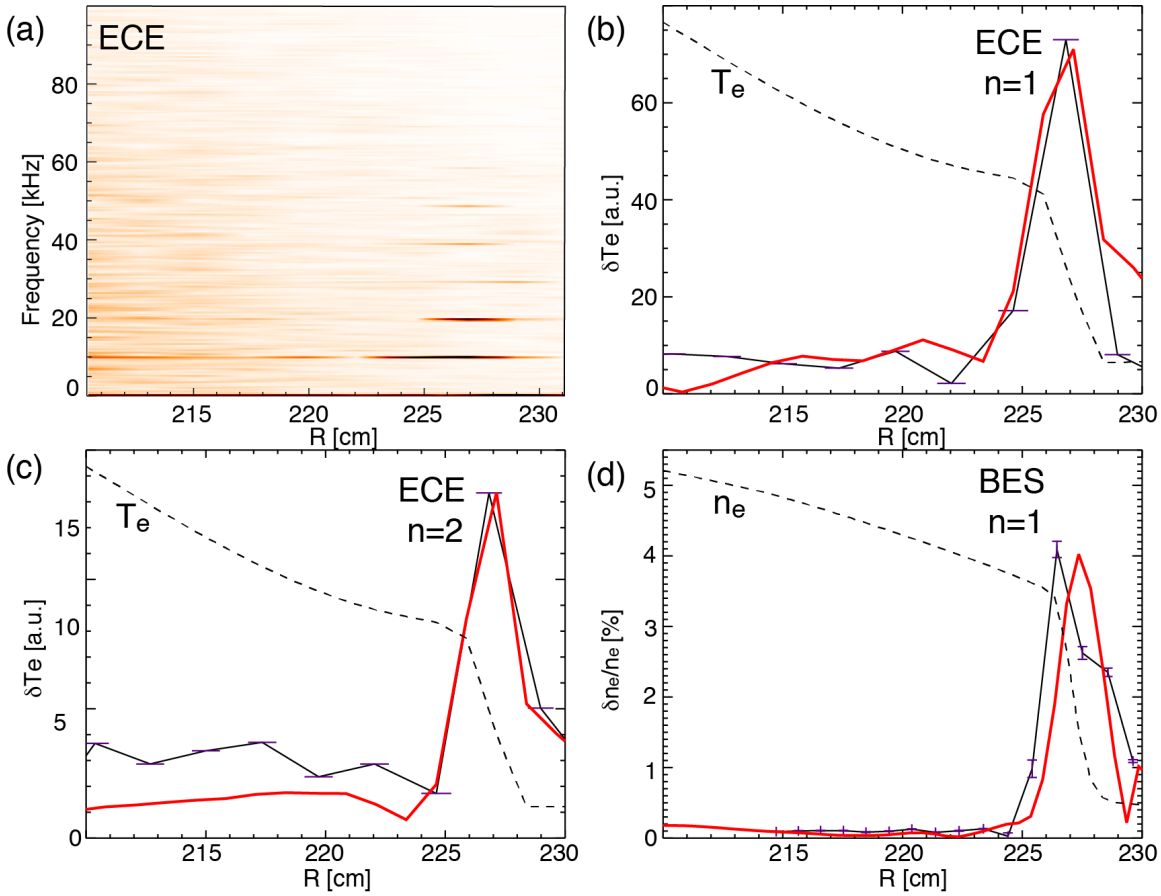
(a)
ECE
Frequency [kHz]
R [cm]
(b)
ECE
n=1
Te
δTe [a.u.]
R [cm]
(c)
ECE
n=2
Te
δTe [a.u.]
R [cm]
(d)
BES
n=1
ne
δne/ne [%]
R [cm]

Chen Fig. 10

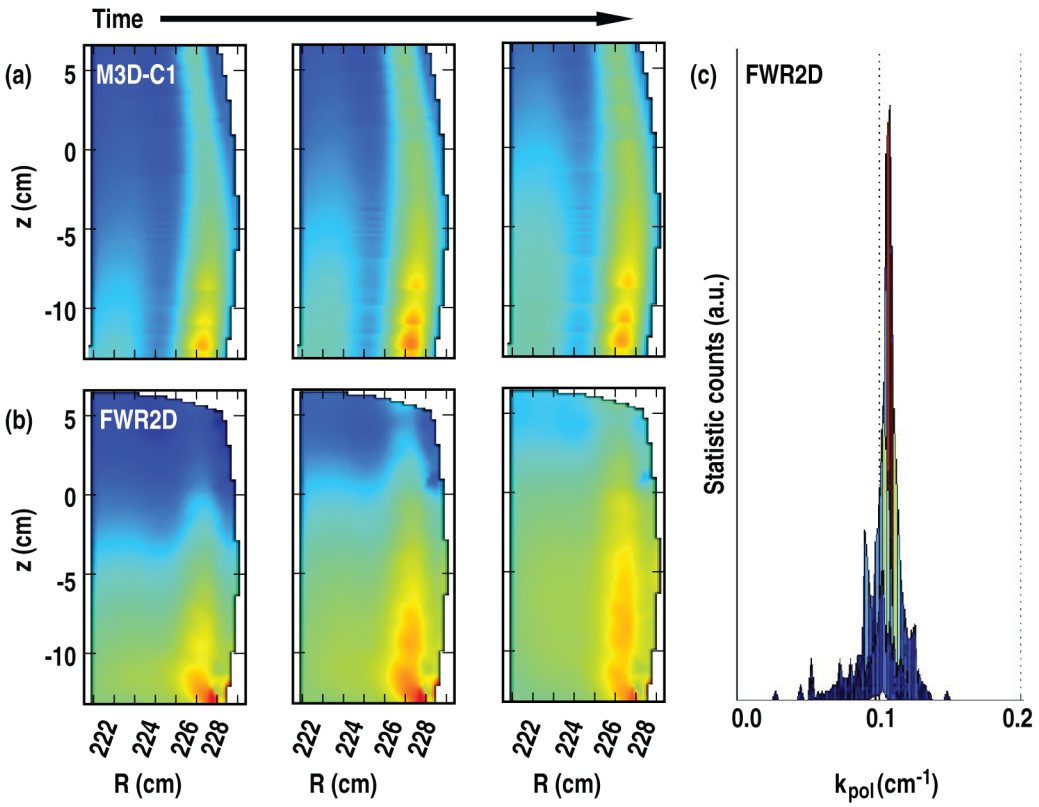
Time
(a)
M3D-C1
(b)
FWR2D
z (cm)
5
0
-5
-10
222
224
226
228
R (cm)
(c)
FWR2D
Statistic counts (a.u.)
0.0
0.1
0.2
k_{pol}(cm^{-1})

Chen Fig. 11

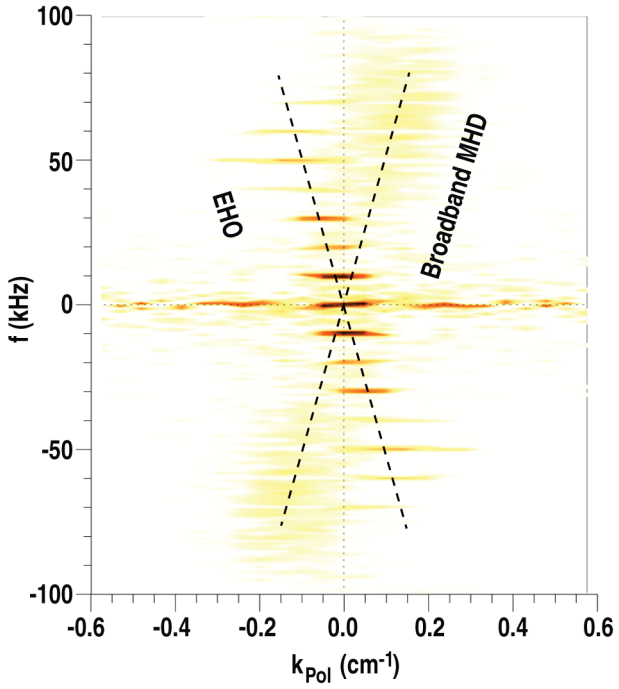
100
50
0
-50
-100
f (kHz)
-0.6
-0.4
-0.2
0.0
0.2
0.4
0.6
k_{Pol} (cm^{-1})
EHO
Broadband MHD

Chen Fig. 12

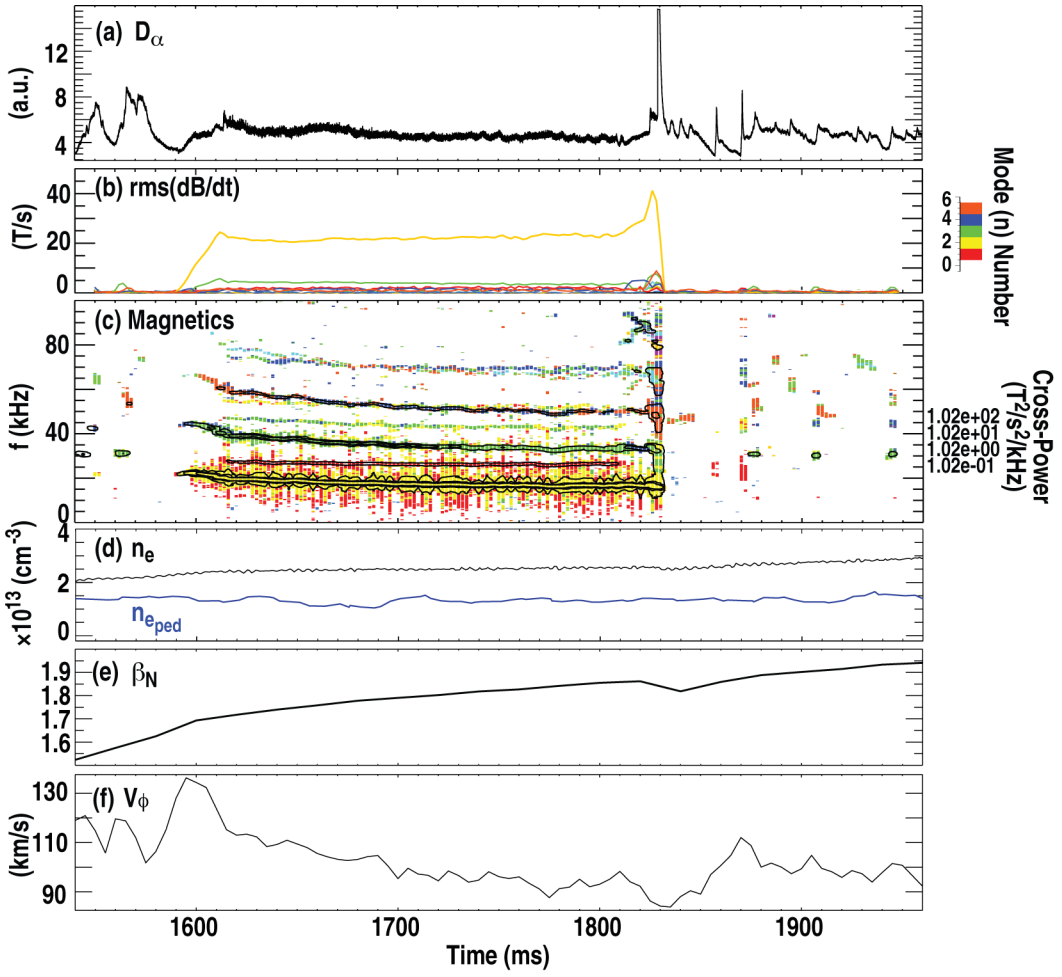
(a) D_α
(a.u.)
12
8
4
(b) rms(dB/dt)
(T/s)
40
20
0
Mode (n) Number
6
4
2
0
(c) Magnetics
f (kHz)
80
40
0
Cross-Power
$(T^2/s^2/kHz)$
1.02e+02
1.02e+01
1.02e+00
1.02e-01
(d) n_e
$n_{e_{ped}}$
$x10^{13}$ (cm^{-3})
4
2
0
(e) β_N
1.9
1.8
1.7
1.6
(f) V_ϕ
(km/s)
130
110
90
1600
1700
1800
1900
Time (ms)

Chen Fig. 13

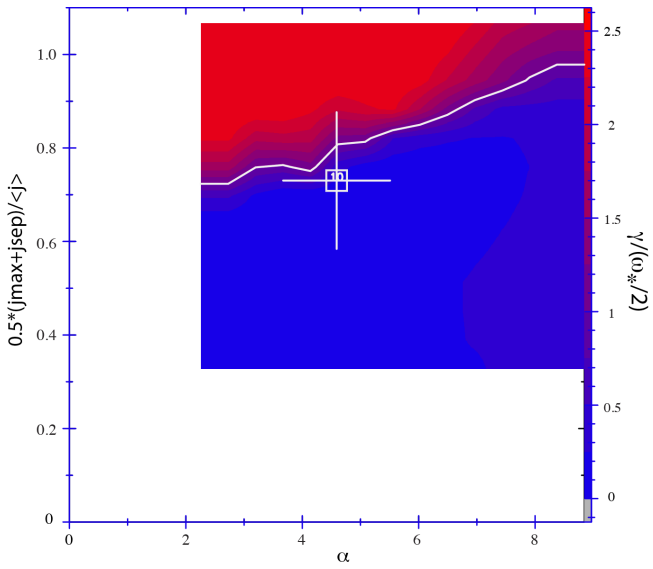

Chen Fig. 14

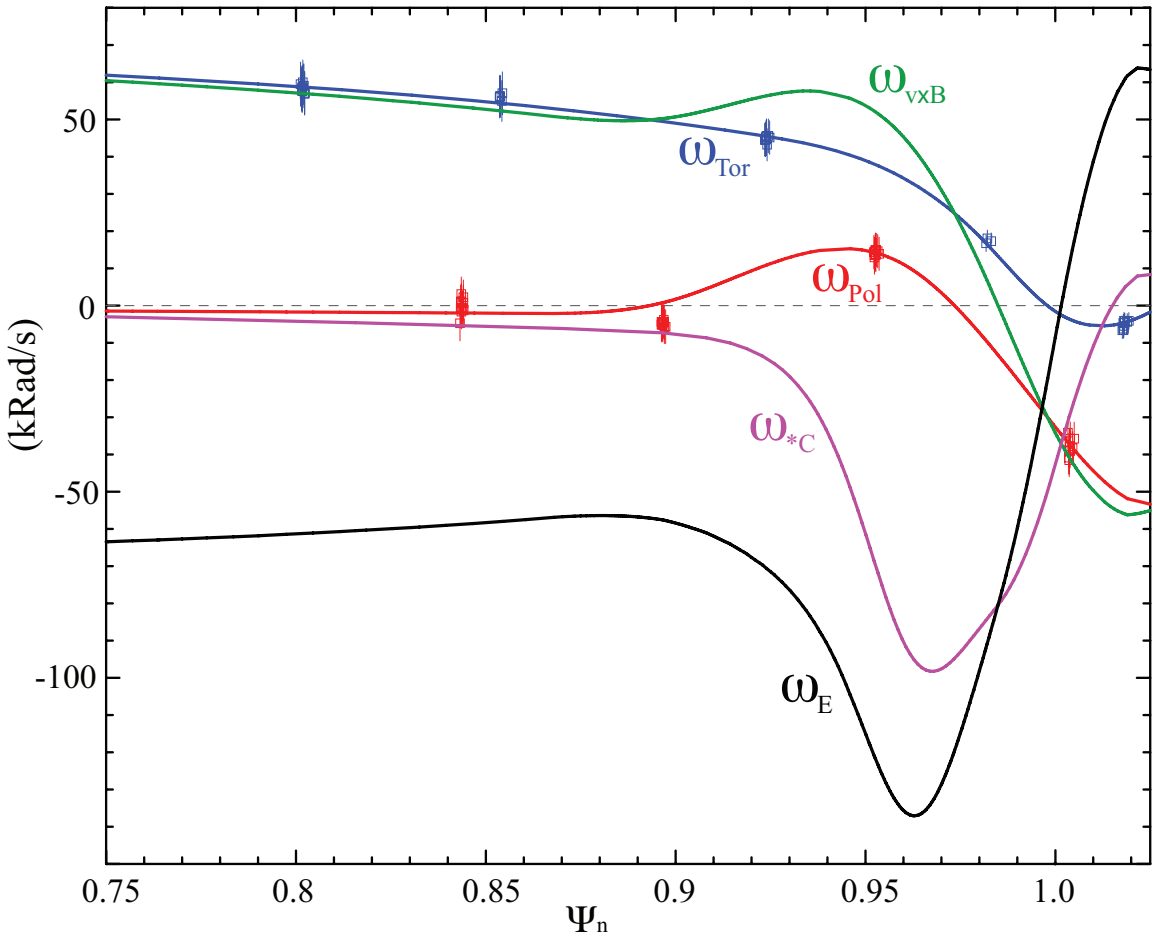

Chen Fig. 15

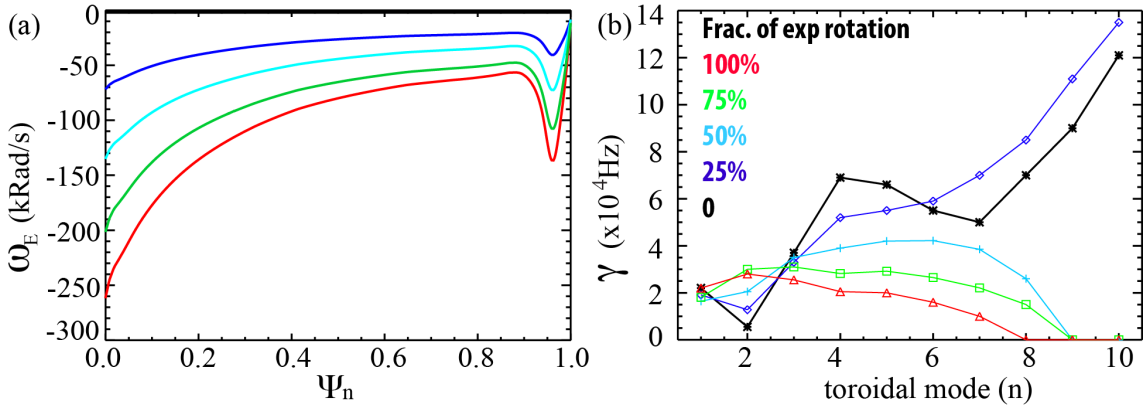
(a)
0
-50
-100
-150
-200
-250
-300
ω_E (kRad/s)
0.0
0.2
0.4
0.6
0.8
1.0
Ψ_n
(b)
14
12
10
8
6
4
2
0
γ (x10^{4}Hz)
Frac. of exp rotation
100%
75%
50%
25%
0
2
4
6
8
10
toroidal mode (n)

Chen Fig. 16